DRAFT VERSION APRIL 8, 2019
Typeset using LaTeX **twocolumn** style in AASTeX62

Fast Outflows Identified in Early Star-Forming Galaxies at $z = 5$–6

YUMA SUGAHARA,[1,2] MASAMI OUCHI,[1,3] YUICHI HARIKANE,[1,2] NICOLAS BOUCHÉ,[4] PETER D. MITCHELL,[5] AND JÉRÉMY BLAIZOT[4]

[1]*Institute for Cosmic Ray Research, The University of Tokyo, 5-1-5 Kashiwanoha, Kashiwa, Chiba 277-8582, Japan*
[2]*Department of Physics, Graduate School of Science, The University of Tokyo, 7-3-1 Hongo, Bunkyo, Tokyo, 113-0033, Japan*
[3]*Kavli Institute for the Physics and Mathematics of the Universe (WPI), University of Tokyo, Kashiwa 277-8583, Japan*
[4]*Univ Lyon, Univ Lyon1, Ens de Lyon, CNRS, Centre de Recherche Astrophysique de Lyon UMR5574, F-69230 Saint-Genis-Laval, France*
[5]*Leiden Observatory, Leiden University, PO Box 9513, NL-2300 RA Leiden, the Netherlands*

Submitted to ApJ

ABSTRACT

We present velocities of galactic outflows in seven star-forming galaxies at $z = 5$–6 with a stellar mass of $M_* \sim 10^{10.1}$ $M_\odot$. Although it is challenging to observationally determine the outflow velocities, we overcome this challenge by making use of the ALMA [C II]158 μm emission lines for systemic velocities and the deep Keck spectra with metal absorption lines for velocity profiles available to date. We construct a composite Keck spectrum of the galaxies at $z = 5$–6 with the [C II]-systemic velocities, and fit outflow-line profiles to the Si II $\lambda1260$, C II $\lambda1335$, and Si IV $\lambda\lambda1394, 1403$ absorption lines in the composite spectrum. We measure the maximum (90%) outflow velocity $v_{\rm max}$ and the central outflow velocity $v_{\rm out}$ to be $v_{\rm max} = 810^{+140}_{-160}$ km s^{-1} and $v_{\rm out} = 440^{+110}_{-140}$ km s^{-1} on average, respectively, showing no significant differences between the outflow velocities derived with the low to high-ionization absorption lines beyond the errors. For $M_* \sim 10^{10.1}$ $M_\odot$, we find the redshift evolution that the $v_{\rm max}$ value of our $z = 5$–6 galaxies is higher than those of $z = 0$ galaxies by a factor of 3.5 and comparable to the one of $z = 2$ galaxies. Estimating the halo circular velocity $v_{\rm cir}$ from the stellar masses and the abundance matching results, we investigate a $v_{\rm max}$–$v_{\rm cir}$ relation. Interestingly, $v_{\rm max}$ for galaxies with $M_* = 10^{10.0-10.8}$ $M_\odot$ shows a clear positive correlation with $v_{\rm cir}$ (as well as the star-formation rate) over $z = 0$–6 with small scatters of $\simeq \pm0.1$ dex, which is in good agreement with the theoretical predictions (Muratov et al. 2015). This positive correlation suggests that the outflow velocity is physically related to the halo circular velocity corresponding to the depth of the gravitational potential, and that the redshift evolution of $v_{\rm max}$ is explained by the increase of $v_{\rm cir}$ toward high redshift.

Keywords: galaxies: formation — galaxies: evolution — galaxies: ISM — galaxies: kinematics and dynamics

1. INTRODUCTION

In actively star-forming galaxies, the energy and momentum inputs from stellar winds and supernovae accelerate the inter-stellar medium (ISM) outwards, and launch galactic-scale outflows. The outflows are composed of the various ISM from cold molecular gas to hot gas (e.g., Veilleux et al. 2005). This mass, momentum, energy, and metal budgets of the outflows leaked from the galaxies are theoretically important for regulating the star-forming activity in the low-mass galaxies, creating the mass-metalicity relation of the galaxies, and polluting the circum-galactic medium and intergalactic medium (IGM) (for a review, see Somerville & Davé 2015). Thus, the outflows in star-forming galaxies have a large impact on the galaxy and IGM evolution.

sugayu@icrr.u-tokyo.ac.jp

In the rest-frame far-ultraviolet (FUV; 1000–2000Å) to optical bands, metal absorption lines are useful to trace the kinematics of the cold and warm outflowing gas. The outflow velocity along the line of sight is estimated with the "down-the-barrel" technique, which measures blueshifts of the absorption lines in the galaxy spectra (e.g., Heckman et al. 2000; Martin 2005; Martin et al. 2012; Rupke et al. 2005a,b; Steidel et al. 2010; Heckman et al. 2015; Chisholm et al. 2015, 2016a, 2017), while the outflowing gas far from the galaxy is detected with the absorption lines in the background-quasar spectra (e.g., Bouché et al. 2012; Kacprzak et al. 2015; Muzahid et al. 2015; Schroetter et al. 2015, 2016). The outflows are ubiquitously observed in the star-forming galaxies at $z < 1.5$ (Weiner et al. 2009; Chen et al. 2010; Rubin et al. 2014). Their outflow velocities are probed to have a positive correlation with the star-formation rate (SFR), the stellar mass (M_*), and the SFR surface rate density ($\Sigma_{\rm SFR}$) (e.g., Rubin et al. 2014; Heckman & Borthakur 2016; Chisholm

et al. 2016b). Sugahara et al. (2017) use archival spectra to show that maximum outflow velocity increases from $z \sim 0$ to 2 in star-forming galaxies that are in a similar M_* and SFR range.

The "down-the-barrel" technique is also appropriate for outflow studies at $z > 2$. Unlike the emission from the outflows whose detection becomes difficult toward high redshift, the absorption can be detected with a bright background continuum source. Shapley et al. (2003) construct composites of almost 1000 Lyman-break galaxy (LBG) spectra at $z \sim 3$ to discuss the relation between the FUV spectral features and the outflow properties. Recently, Du et al. (2018) report no evolution of central outflow velocities at $z \sim 2$–4 using composites of the rest-frame FUV spectra presented in Steidel et al. (2003, 2004), Reddy et al. (2008), and Jones et al. (2012). Although the Lyα profile provides us the information on the neutral-gas kinematics around Lyman alpha emitters at high redshift (e.g., Erb et al. 2014; Shibuya et al. 2014; Hashimoto et al. 2015; Trainor et al. 2015; Karman et al. 2017), even at $z \sim 6$ (Ajiki et al. 2002), it is difficult to directly estimate the outflow properties only from the Lyα profile due to its strong resonance scattering.

One of the keys to estimate outflow properties is to determine the systemic redshifts of the galaxies. At the low redshift, the systemic redshifts are measured by nebular emission lines (e.g., Hα, [O III], and [O II]), but observations of the emission lines become expensive at high redshift. Some outflow studies at $z > 1.5$ conduct additional near-infrared (IR) observations (Steidel et al. 2010; Shibuya et al. 2014), while others determine the redshifts from Lyα emission or interstellar absorption, which includes the uncertainties based on the outflows (Shapley et al. 2003; Du et al. 2018). Moreover, a precise measurement of the systemic redshifts is challenging at $z > 5$, where the strong optical emission lines fall into the mid-IR bands. Although there are several nebular emission lines in the rest-frame FUV band such as O III]$\lambda\lambda$1660, 1666 and C III]$\lambda\lambda$1906, 1908, these lines are weak to be detected in typical star-forming galaxies at high redshift. This problem makes it difficult to extend the outflow studies to $z > 5$.

A solution in this paper is observations with the Atacama Large Millimeter/submillimeter Array (ALMA). Recent ALMA observations detect [C II] 158 μm and [O III] 88 μm emission lines in high-z galaxies (e.g., Capak et al. 2015; Inoue et al. 2016; Hashimoto et al. 2018), which enables us to measure the systemic redshifts of the galaxies. Combining the redshift determined from the ALMA observations with deep observed-frame optical spectra, we can address the outflow properties at $z > 5$. As a case study, Pavesi et al. (2016) discuss the rest-frame FUV absorption lines in HZ10, a IR-luminous LBG at $z \simeq 5.6$, and find the blueshifts with respect to the [C II] emission line.

This paper presents estimates of outflow velocities in star-forming galaxies at $z = 5$–6 and discuss the redshift evolution of the outflows from $z \sim 0$ to 6. Section 2 describes the sample of galaxies at $z = 5$–6. Section 3 explains the analysis of the absorption lines in the observed-frame optical spectra. We obtain a composite spectra of the galaxies to measure the outflow velocity. Section 4 shows the results on the outflow velocity and its redshift evolution. Section 5 discusses relations between the outflow and galaxy properties. Section 6 summarizes our conclusion. The ΛCDM cosmology is used throughout this paper: $\Omega_{\rm M} = 0.27$, $\Omega_\Lambda = 0.73$, $h = H_0/(100\ {\rm km\ s^{-1}\ Mpc^{-1}}) = 0.70$, $n_s = 0.95$, and $\sigma_8 = 0.82$. All transition are referred to by their wavelengths in vacuum.

2. SAMPLE AND DATA REDUCTION

Our sample consists of seven galaxies at $z = 5$–6 whose spectra are taken in the optical and millimeter wavelengths. We use the galaxies presented in Capak et al. (2015), who observe nine LBGs and one low-luminosity quasar at $z \sim 5$–6 in the Cosmic Evolution Survey (COSMOS; Scoville et al. 2007) field. Capak et al. (2015) obtain the rest-frame FUV spectra of the galaxies with the DEep Imaging Multi-Object Spectrograph (DEIMOS; Faber et al. 2003) at the Keck II telescope. The spectroscopic configuration is the 830 lines mm^{-1} grating with the OG550 filter, which gives the wavelength coverage of 6000–9500 Å and the spectral resolution of $R \sim 2500$–3500. The total integration time is ∼3.5 hr for each object.

We download the raw DEIMOS data of the galaxies from the Keck Observatory Archive[1] (KOA). The raw data are reduced with the `IDL` package, the DEIMOS `spec2d` pipeline, developed by the Deep Extragalactic Evolutionary Probe 2 (DEEP2) Redshift Survey team (Cooper et al. 2012; Newman et al. 2013). From the reduced two-dimensional data, the pipeline extracts the one-dimensional spectra of the science targets. Finally, we obtain the rest-frame FUV spectra of seven out of the nine LBGs in Capak et al. (2015), excluding two spectra that we cannot identify from the reduced data.

The ALMA follow-up observations are conducted in a project of #2012.1.00523.S (PI: P. Capak). The Band 7 observations have detected the [C II] emission lines in all of the nine LBGs. In this study, we use the systemic redshifts that are estimated from the [C II] emission lines by Capak et al. (2015). The median redshift error is $\sim 2\times10^{-4}$, corresponding to ~ 10 km s^{-1}. The systemic redshifts of our galaxies are listed in Table 1.

We use SFR and M_* derived by Capak et al. (2015). The SFR is estimated from the sum of the rest-frame UV and IR luminosity. The stellar mass M_* is estimated from the spectral energy distribution fitting to the optical to IR photometry taken from the COSMOS photometric redshift catalog (Ilbert et al. 2013) and the Spitzer-Large Area Survey with Hyper-Suprime-Cam (SPLASH; Steinhardt et al. 2014). The halo circular velocity $v_{\rm cir}$ is estimated from M_*. After converting M_* into the halo mass $M_{\rm h}$ with the stellar-to-halo mass ratio (SHMR) given by Behroozi et al. (2013), we calculate $v_{\rm cir}$

[1] KOA website: http://www2.keck.hawaii.edu/koa/public/koa.php.

Table 1. Galaxy properties of seven LBGs

name	R.A.	Decl.	S/N of DEIMOS spectra (pixel^{-1})	$z_{\rm sys}$[a]	$z_{\rm sys}$ error (km s^{-1})	$\log(M_*/M_\odot)$
HZ1	09:59:53.25	02:07:05.43	0.348115	5.6885	9	10.47 ± 0.13
HZ2	10:02:04.10	01:55:44.05	0.455985	5.6697	30	10.23 ± 0.15
HZ4	09:58:28.52	02:03:06.74	0.616747	5.5440	9	9.67 ± 0.21
HZ6	10:00:21.50	02:35:11.08	0.776667	5.2928	5	10.17 ± 0.15
HZ7	09:59:30.48	02:08:02.81	0.275164	5.2532	20	9.86 ± 0.21
HZ8	10:00:04.06	02:37:35.81	0.216720	5.1533	10	9.77 ± 0.15
HZ10	10:00:59.30	01:33:19.53	0.625486	5.6566	9	10.39 ± 0.17

NOTE—The raw DEIMOS spectra are downloaded from KOA (PI: P. Capak). The $z_{\rm sys}$ and M_* values are drawn from Capak et al. (2015).

[a]The systemic redshift $z_{\rm sys}$ is determined by the [C II] 158 μm emission line taken by ALMA.

by equations in Mo & White (2002) expressed as

$$v_{\rm cir} = \left(\frac{GM_{\rm h}}{r_{\rm h}}\right)^{1/2}, \quad (1)$$

$$r_{\rm h} = \left(\frac{GM_{\rm h}}{100\Omega_{\rm M}H_0^2}\right)^{1/3}(1+z)^{-1}, \quad (2)$$

where G is the gravitational constant and $r_{\rm h}$ the halo radius.

3. ANALYSIS AND MEASUREMENTS

Since the outflowing gas gives rise to the blueshifted metal absorption lines due to the Doppler shift, the blueshift reflects the line-of-sight velocity of the outflowing gas. The absorption-line analysis requires high signal-to-noise ratios (S/N) of the continuum spectra. Our rest-frame FUV spectra have the average S/N of $\simeq 0.47$ pixel^{-1}, which is not enough for the absorption-line analysis. Therefore, we obtain a high-S/N composite spectrum by stacking all of the spectra with an inverse-variance weighted mean. The top panel of Figure 1 shows the composite spectrum and its error spectrum. The continuum S/N of the composite spectrum is 1.4 pixel^{-1} around the Si II λ1260 absorption line. The physical parameters of the composite spectrum are truncated mean discarding the maximum and minimum values. In the wavelength range from 1150 to 1450 Å in the rest frame, we use the absorption lines of Si II λ1260, C II λ1335, and Si IV $\lambda\lambda$1394, 1403 for the analysis, without the Si II λ1304 line that has a nearby strong O I λ1302 absorption line. We hereafter refer to Si II λ1260 as Si II.

We measure outflow velocities by fitting a line profile to the absorption lines. As the line profile, we adopt a physical profile based on the assumption of the curve of growth (Rupke et al. 2005a). This line profile $I(\lambda)$, as a function of the wavelength λ, is expressed by

$$I(\lambda)/I_0 = 1 - C_f + C_f \exp(-\tau(\lambda)), \quad (3)$$

$$\tau(\lambda) = \tau_0 \exp(-(v - v_0)^2/b^2), \quad (4)$$

where I_0 is the continuum level, C_f the covering fraction, $\tau(\lambda)$ the optical depth, τ_0 the optical depth at the line center, v the velocity measured from the rest wavelength, v_0 the velocity at the line center, and b the Doppler width. The line profile is convolved with a Gaussian profile representing the spectral resolution. The free parameters are five: I_0, v_0, C_f, τ_0, and b_D. Since the composite spectrum has large noises, we treat I_0 as a free parameter instead of normalizing the spectrum by a stellar continuum. We fit the line profile to Si II, C II, and Si IV, using an `IDL` procedure `MPFIT`, which performs non-linear least-squares fitting in a robust manner (Markwardt 2009). The bottom panel of Figure 1 shows the best-fit model of the Si II, C II, and Si IV absorption lines with the red lines.

The best-fit v_0 values, listed in Table 2, are all significantly negative, implying that the absorption lines are blueshifted by the outflowing gas. These velocities are consistent with the literature. HZ10 has the Si II, Si II λ1304/O I, and Si IV absorption lines blueshifted by 100 ± 180 km s^{-1} with respect to the [C II] emission line (Pavesi et al. 2016). The composite emission of the [C II] line in HZ1–10 is reported to have the broad wings that are likely generated by the outflows with the velocity of $\sigma = 100$–500 km s^{-1} (Gallerani et al. 2018)

We define the maximum outflow velocity $v_{\rm max}$ as

$$v_{\rm max} = -v_0 + b\sqrt{-\ln\left(\frac{1}{\tau_0}\ln\frac{1}{0.9}\right)}, \quad (5)$$

which represents the velocity where the best-fit model has a $(100 - 10C_f)\%$ flux of the continuum[2]. The error of $v_{\rm max}$ is evaluated by the parametric bootstrap method. We obtain the $v_{\rm max}$ distribution from the 1000 resampling fluxes based on the spectral noise and use the $\pm$34th $v_{\rm max}$ values for its error.

The derived maximum outflow velocities for Si II, C II, and Si IV are $v_{\rm max}^{\rm SiII} = 730^{+260}_{-140}$ km s^{-1}, $v_{\rm max}^{\rm CII} = 790^{+110}_{-340}$ km s^{-1}, and $v_{\rm max}^{\rm SiIV} = 630^{+220}_{-84}$ km s^{-1}, respectively. Low-ionized elements (Si II and C II) have ionization potentials

[2] Throughout this paper, $v_{\rm max}$ is not the maximum circular velocity in the rotation curve of a galaxy or halo, which is often used in theoretical papers.

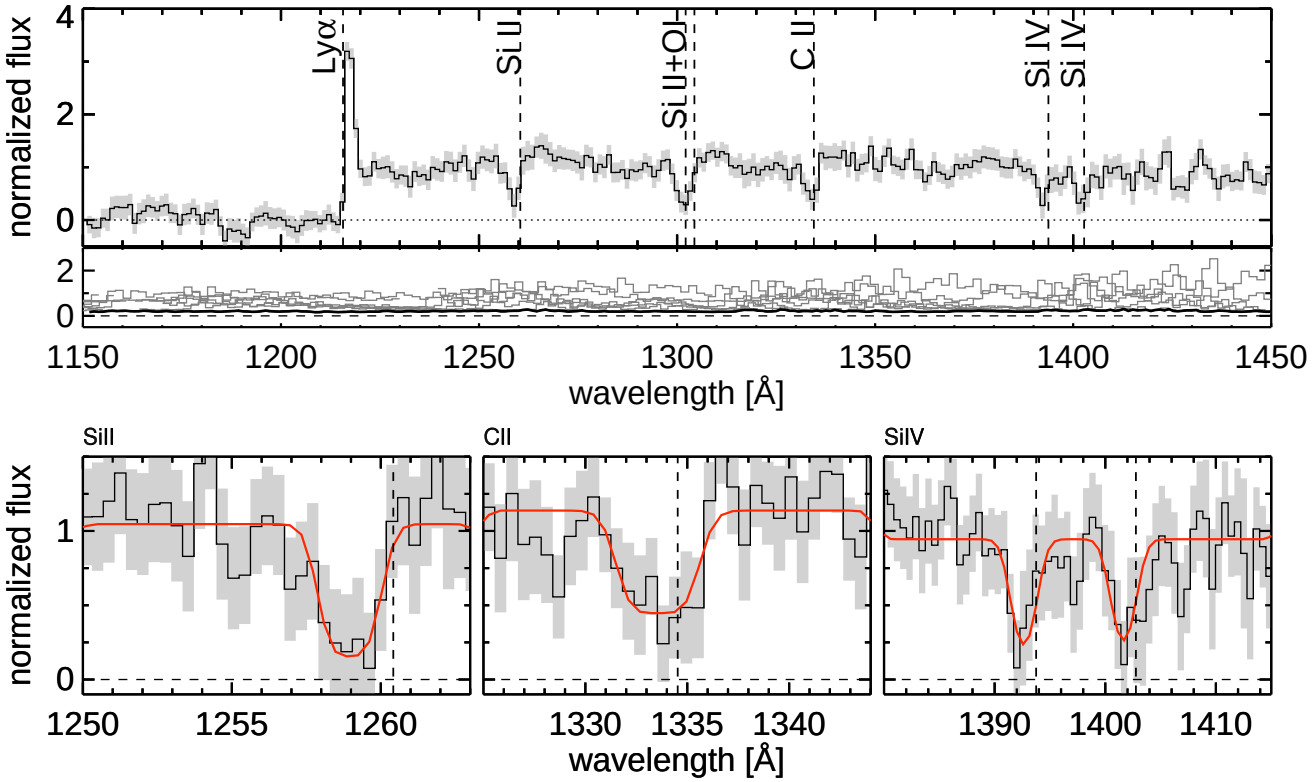

Figure 1. Top: composite spectrum of our sample. The gray shade indicates the 1σ error at each pixel. The spectral resolution is smoothed for the display purpose. The rest wavelengths of the emission and absorption lines are plotted with the dashed vertical lines. The second panel under the main panel shows the 1σ error spectra. The gray and black lines denote the errors of the normalized individual spectra and the composite spectrum, respectively. The wavelengths of the individual spectra are corrected to the rest frame using the systemic redshift determined by ALMA [C II] observation. Bottom: Si II, C II, and Si IV absorption lines from left to right. The red solid lines are the best-fit absorption model. The vertical and horizontal dashed lines denote the rest wavelengths of the absorption lines and zero flux, respectively.

Table 2. Measured outflow velocities for the absorption lines

redshift	line	v_0 (km s^{-1})	$v_{\rm max}$ (km s^{-1})
$z = 5$–6	Si II λ1260	-366^{+63}_{-99}	730^{+260}_{-140}
...	C II λ1335	-210^{+120}_{-74}	790^{+110}_{-340}
...	Si IV $\lambda\lambda$1394, 1403	-220^{+150}_{-100}	630^{+220}_{-84}
...	Si II & C II	-	810^{+140}_{-160}
$z \sim 2$[a]	C II λ1335	$-134^{+9.6}_{-8.6}$	706^{+31}_{-38}

[a] We obtain the velocities at $z \sim 2$ by re-analyzing the composite spectrum of Sugahara et al. (2017).

lower than that of hydrogen (13.6 eV), while high-ionized elements (Si IV) have a much higher ionization potential. Although the low- and high-ionized elements trace the different state of the ISM, $v_{\rm max}^{\rm SiII}$ and $v_{\rm max}^{\rm CII}$ are consistent with $v_{\rm max}^{\rm SiIV}$ within the 1σ errors. This consistency agrees with previous work on outflows at $z \sim 0$ (Chisholm et al. 2016b).

Si II and C II have similar ionization potentials and oscillator strengths, and exhibit similar maximum outflow velocities. To obtain a typical $v_{\rm max}$ value of the $z = 5$–6 galaxies, we additionally measure the maximum outflow velocity by a simultaneous fitting to Si II and C II, adopting $v_{\rm max}$ as a free parameter instead of v_0. Both lines are assumed to have the same C_f. The measured value is $v_{\rm max} = 810^{+140}_{-160}$ km s^{-1}. This value is consistent with $v_{\rm max}^{\rm SiII}$ and $v_{\rm max}^{\rm CII}$, but its error is smaller than those of $v_{\rm max}^{\rm SiII}$ and $v_{\rm max}^{\rm CII}$. Table 2 lists the measurements of $v_{\rm max}$ and v_0 for each absorption lines.

4. RESULTS

4.1. *Maximum Outflow Velocity vs. Galaxy Properties*

Comparing our measurements of $v_{\rm max}$ at $z = 5$–6 with those at low redshifts, we study the redshift evolution of the outflow velocity. For $v_{\rm max}$ at low redshifts, we use the values at $z \sim 0$–2 given by Sugahara et al. (2017), who obtain outflow properties using spectra of Sloan Digital Sky Survey Data Release 7 (SDSS DR7; Abazajian et al. 2009) at $z \sim 0$, DEEP2 DR4 survey (Newman et al. 2013) at $z \sim 1$, and Keck spectra in Erb et al. (2006) at $z \sim 2$. Sugahara et al. (2017) basically perform the same analysis as we have done, but for a two-component absorption-line profile that consists of a systemic component fixed at the systemic velocity and a blueshifted component produced by the outflow-

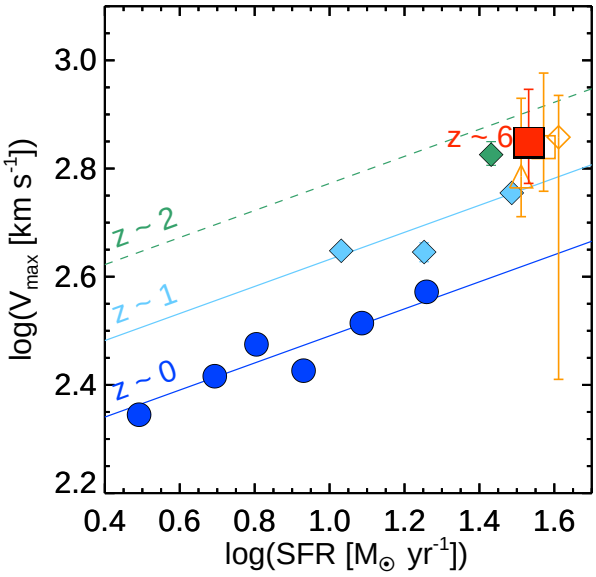

Figure 2. Maximum outflow velocity $v_{\rm max}$ as a function of SFR over $z \sim$ 0–6. The filled red square indicates the $v_{\rm max}$ value at $z =$ 5–6 measured with the simultaneous fitting of the Si II and C II lines. The open orange square, diamond, and triangle represent the values measured for Si II, C II, and Si IV, respectively. The data points at $z \sim 0$ (blue) and $z \sim 1$ (cyan) are presented by Sugahara et al. (2017). The blue circles are measured for Na I D and the cyan diamonds for Mg II. The $v_{\rm max}$ value at $z \sim 2$ is re-calculated in the manner of this work, denoted by the green diamond. The error bars show 1σ measurement errors. The blue, cyan, and green lines express the best-fit relation at $z \sim$ 0, 1, and 2, respectively, whose slopes are fixed at the best-fit slope at $z \sim 0$. Since the $z \sim 2$ best-fit relation is the one in Sugahara et al. (2017), there is a offset between the green diamond and the green dashed line.

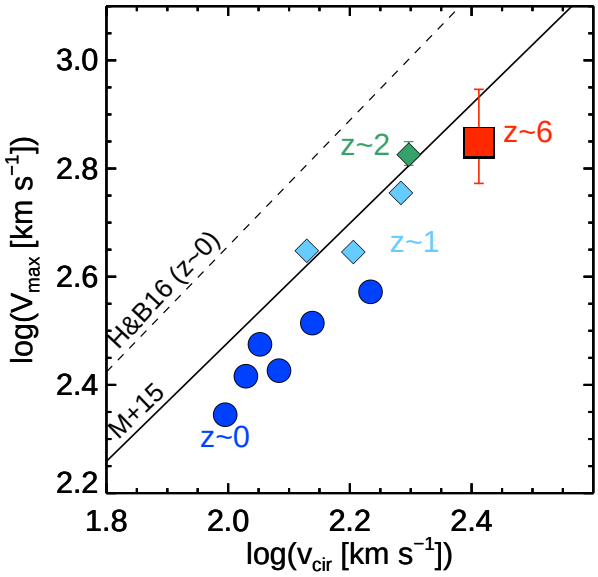

Figure 3. $v_{\rm max}$ as a function of the circular velocity $v_{\rm cir}$ that are converted from the stellar mass. The symbols are the same as in Figure 2. The solid line represents a theoretical relation predicted by the FIRE simulation (the flux-weighted average 90th percentile velocity; Muratov et al. 2015). The dashed line indicates a relation of extreme-starburst galaxies $z \sim 0$ Heckman & Borthakur (2016).

ing gas. This difference in the methods is negligible for the spectra at $z \sim 0$ and 1, where the absorption lines have small systemic components (Sugahara et al. 2017). The spectra at $z \sim 2$, however, have large systemic components. Therefore, we re-analyze the absorption lines of the normalized composite spectrum at $z \sim 2$ to measure the maximum outflow velocity with the one-component absorption-line profile described in Section 3. The new maximum outflow velocity becomes lower than the previous value, but the conclusions in Sugahara et al. (2017) are not affected by this re-analysis.

Figure 2 shows the maximum outflow velocity as a function of SFR. The $v_{\rm max}^{\rm SiII}$, $v_{\rm max}^{\rm CII}$, $v_{\rm max}^{\rm SiIV}$, and $v_{\rm max}$ values are plotted with the open orange square, diamond, triangle, and filled red square, respectively. Sugahara et al. (2017) illustrate that the outflow velocity increases from $z \sim 0$ (blue) to 2 (green) in star-forming galaxies with similar M_* and SFR. We find that the $v_{\rm max}$ value at $z =$ 5–6 is $\sim$ 0.2 dex higher than the relation at $z \sim 0$ and comparable to the value at $z \sim 2$. This means that the outflow velocity shows a strong increase from $z \sim 0$ to 2 and a slight or no increase from $z \sim 2$ to 6 in galaxies with similar M_* and SFR.

Figure 3 illustrates $v_{\rm max}$ as a function of the halo circular velocity ($v_{\rm cir}$) that are calculated from M_* in Section 2. In the figure, $v_{\rm max}$ tightly correlates with $v_{\rm cir}$ at $z \sim 0$. A correlation with a similar slope at $z \sim 0$ is also seen in the cyan diamonds at $z \sim 1$. Although only one measurement is available at $z \sim 2$ and $z =$ 5–6, respectively, the two data points at $z \sim$ 2–6 appear to follow the relation at $z \sim$ 0–1. Therefore, Figure 3 suggests a single relation between $v_{\rm max}$ and $v_{\rm cir}$ that holds over $z \sim$ 0–6. The dashed line indicates a relation at $z = 0$ obtained from observations by the Cosmic Origin Spectrograph mounted on the Hubble Space Telescope (Heckman & Borthakur 2016), which has a similar slope to our measurements. The offset between our data points and the solid line may arise from the fact that our data points represent the average properties of galaxies at each redshift while their extreme-starburst galaxies have much higher SFR than our galaxies with a similar $v_{\rm cir}$.

4.2. *Redshift evolution of outflow velocities*

We illustrate the redshift evolution of $v_{\rm max}$ in star-forming galaxies with $M_* \sim 10.1$ M$_\odot$ in the top panel of Figure 4. As shown in Section 4.1, $v_{\rm max}$ strongly increases from $z \sim 0$ to 2 and slightly from $z \sim 2$ to 6. The crosses in the figure indicate the maximum outflow velocity of the gravitationally lensed sources presented in Jones et al. (2013). The stellar

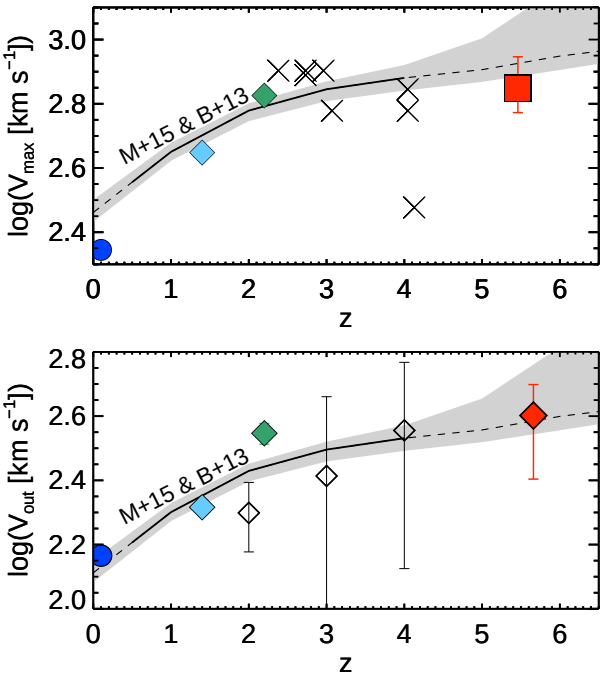

Figure 4. Redshift evolution of $v_{\rm max}$ (top) and $v_{\rm out}$ (bottom) in the star-forming galaxies with $M_* \sim 10^{10.1}$ $M_\odot$. The colored symbols are the same as in Figure 2, but for the red diamond that denotes $v_{\rm out}$ of the galaxies at $z = 5$–6 measured by a fit of the two-component Gaussian profile to the C II line. To compare the literature, we plot the values of the individual gravitationally-lensed sources in Jones et al. (2013, cross) and the composite spectra at $z \sim 2$, 3, and 4 presented by Du et al. (2018, open diamond), including galaxies with $M_* < 10^{10.1}$ $M_\odot$. The solid lines indicate the evolution of the flux-weighted 90th (top) and 50th (bottom) outflow velocities that we estimate based on the velocity–$v_{\rm cir}$ relation at $z = 0.5$–4 in the FIRE simulation (Muratov et al. 2015) at the fixed M_* using the SHMR of Behroozi et al. (2013). The evolution is extrapolated to $z < 0.5$ and $z > 4$ (dashed line) and the errors of the SHMR are shown in the shaded regions.

mass of these sources is not derived and the outflow velocity of them is measured in a different manner from ours. However, the sources have similar $v_{\rm max}$ values to our $v_{\rm max}$ values at $z \sim 2$ and $z = 5$–6, except for a data point of $v_{\rm max} \simeq 300$ km s^{-1}. While Jones et al. (2013) suggest a decrease in $v_{\rm max}$ at high redshift that are not statistically significant, we do not find the decrease at $z = 5$–6.

Sugahara et al. (2017) and Du et al. (2018) discuss the redshift evolution of the central outflow velocity ($v_{\rm out}$) measured with a two-component profile. To check the evolution at $z = 5$–6, we measure $v_{\rm out}$ from the composite spectrum at $z = 5$–6 by fitting a two-component Gaussian profile to the C II absorption line, although the errors of the best-fit values become larger than those obtained with a one-component-profile fitting. The two-component Gaussian profile consists

Table 3. Values of the data points at each redshift in Figure 4

redshift	$v_{\rm out}$ (km s^{-1})	$v_{\rm max}$ (km s^{-1})	$\log(M_*/M_\odot)$[a]	reference
$z \sim 0$	146 ± 5.2	221 ± 9.9	10.2	S17
$z \sim 1$	207 ± 5.0	445 ± 5.7	10.0	S17
$z \sim 2$	352^{+26}_{-27}[b]	673^{+35}_{-33}[b]	10.3	S17
$z = 5$–6	440^{+110}_{-140}	810^{+140}_{-160}	10.1	This study

[a] The mean stellar mass of the galaxies.

[b] The outflow velocities at $z \sim 2$ are re-measured in this study.

References—S17: Sugahara et al. (2017)

of the systemic and outflow components; $v_{\rm out}$ is defined as the central velocity of the outflow component. This analysis is identical to that used in Du et al. (2018). Before the fitting, the composite spectrum is smoothed by a Gaussian kernel so that the spectral resolution become similar to the composite spectrum at $z \gtrsim 2$ in Sugahara et al. (2017) and Du et al. (2018). We also analyze the composite spectrum at $z \sim 2$ presented in Sugahara et al. (2017).

The measured velocities are $v_{\rm out} = 440^{+110}_{-140}$ km s^{-1} at $z = 5$–6 and $v_{\rm out} = 352^{+26}_{-27}$ km s^{-1} at $z \sim 2$. The bottom panel of Figure 4 shows the redshift evolution of $v_{\rm out}$. We find that the $v_{\rm out}$ evolution has similar features to the $v_{\rm max}$ evolution: a strong increase from $z \sim 0$ to 2 and no increase from $z \sim 2$ to 6 within the errors. The latter is consistent with a result of Du et al. (2018). The $v_{\rm max}$ and $v_{\rm out}$ values at $z \sim 0$, 1, 2, and 5–6 are listed in Table 3.

The open diamonds indicate $v_{\rm out}$ at $z \sim 2$, 3, and 4 given by Du et al. (2018). The $v_{\rm out}$ value at $z = 5$–6 is comparable to those at $z \sim 3$ and 4 within the marginally large error bars. However, the value at $z \sim 2$ denoted by the green diamond is not consistent with the one denoted by the open diamond. In addition, the error bars of the open diamonds are generally larger than those of the filled symbols, in spite of the fact that Du et al. (2018) stacked a larger number of galaxy spectra than this study and Sugahara et al. (2017). These results may be attributed to the uncertainty of the systemic redshifts in Du et al. (2018), who determine the systemic redshifts from the Lyα emission or interstellar absorption lines. When individual spectra are stacked using the systemic redshifts, the uncertainties of the systemic redshifts broaden absorption lines in the composite spectrum. It is possible that this broad absorption line produces large errors in the best-fit parameters of the two-component fitting that are sensitive to the absorption-line profile. We note that the median stellar masses of the galaxies in Du et al. (2018) are $\log(M_*/M_\odot) = 10.00$, 9.87, and 9.72 at $z \sim 2$, 3, and 4, respectively, which are less than M_* of our galaxies. It is also possible that this small M_* (i.e., small $v_{\rm cir}$) may lead to the low $v_{\rm out}$ value at $z \sim 2$.

5. DISCUSSION

5.1. *Comparisons with theoretical models*

Recent zoom-in simulations can be used to predict an outflow velocity. Muratov et al. (2015) calculate the flux-weighted velocity of the outflowing gas at 0.25 halo virial radius with the Feedback in Realistic Environments (FIRE) simulation, which computes the thermal and momentum input to the ISM considering the stellar and supernova feedback. The outflow velocity in the FIRE simulation tightly correlates with the halo circular velocity and the correlation does not exhibit the significant evolution over $z \sim 0.5$–4.

In Figure 3 we present the tight linear relation between $v_{\rm max}$ and $v_{\rm cir}$. The solid line in the figure denotes the relation predicted by Muratov et al. (2015). Their theoretical prediction at $z = 0.5$–4 is surprisingly in good agreement with our observational results at $z = 0$–6, although the outflow velocity at $z \sim 0$ is ~ 0.1 dex lower than the theoretical prediction. This agreement theoretically supports our result that $v_{\rm max}$ correlates with $v_{\rm cir}$. We note that as described in Section 3 our observational technique traces low-ionized elements that are included in warm gas ($\lesssim 10^4$ K). On the other hand, Muratov et al. (2015) do not present measurements of outflowing gas in a given phase; they compute the outflow velocity from outflowing gas with all temperatures. Since the bulk of the outflows in the numerical simulation would not be in a phase of the observed outflows, the agreement perhaps suggests that multi-phase outflows are accelerated following a common $v_{\rm max}$–$v_{\rm cir}$ relation, irrespective of gas phases.

In Figure 4 the black solid line indicates the redshift evolution of the outflow velocity based on the results given by the FIRE simulation (Muratov et al. 2015), where we convert $v_{\rm cir}$ to M_* using the SHMR of Behroozi et al. (2013) and Equation (1). The evolution based on Muratov et al. (2015) is in good agreement with the $v_{\rm max}$ and $v_{\rm out}$ values in this study and Sugahara et al. (2017), and also with those in Du et al. (2018) and Jones et al. (2013), except for one at $z \sim 4$.

This good agreement supports a monotonic increase in $v_{\rm max}$ from $z = 0$ to 6 that is driven by a monotonic increase in $v_{\rm cir}$. While $M_{\rm h}$ does not significantly change around $M_* \sim 10.1$ M$_\odot$ at $z \sim 0$–6 (Behroozi et al. 2013), $r_{\rm h}$ is proportional to $(1+z)^{-1}$ at a fixed M_h (Equation 2). Hence, Equation (1) gives the redshift dependence of the halo circular velocity as $v_{\rm cir} \propto (1+z)^{0.5}$. Given that $v_{\rm max}$ has the linear correlation with $v_{\rm cir}$ as shown in Figure 3, the redshift evolution in $v_{\rm max}$ (Figure 4) is explained as reflecting the redshift dependence of $v_{\rm cir}$. The power-law index of 0.5 reproduces the strong increase in $v_{\rm max}$ from $z \sim 0$ to 2 and the slight increase from $z \sim 2$ to 6.

5.2. *Outflow-velocity correlation with* SFR *and* SFR$/M_*$

The outflow maximum velocity tightly correlates with the halo circular velocity, but it also has a strong correlation with SFR. It is worth discussing correlations of $v_{\rm max}$ with galaxy properties over the wide redshift range. Figure 5 plots $v_{\rm max}$ as a function of $v_{\rm cir}$, SFR, M_*, and SFR$/M_*$. First, we calculate the Spearman's rank correlations, r, between $v_{\rm max}$ and the galaxy properties. While M_* has no correlation with $v_{\rm max}$, the other galaxy properties exhibit strong correlations

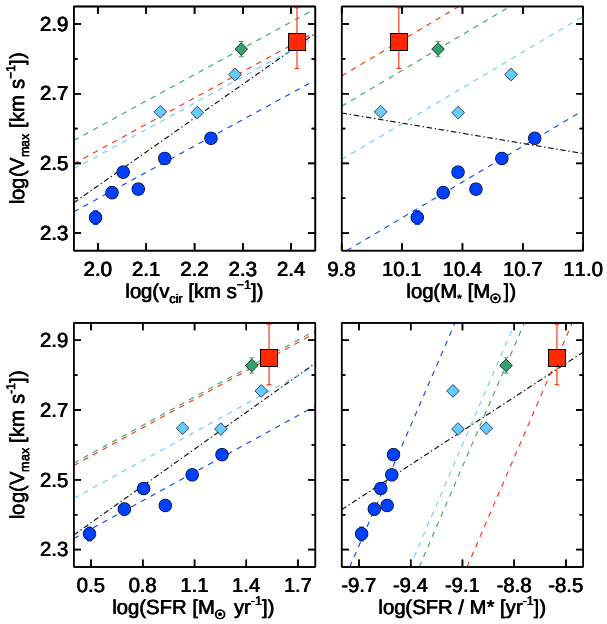

Figure 5. Correlations between $v_{\rm max}$ and galaxy properties. The symbols are the same as in Figure 2. Dashed lines indicate the best-fit linear relations to the data points at each redshift. The slopes of the relations at $z \sim 1$ (cyan), 2 (green), and 5–6 (red) are fixed at the value at $z \sim 0$ (blue), which is determined as a free parameter. The black dot-dashed lines denote the best-fit linear relations to the all data points.

of $r = 0.81$ ($v_{\rm cir}$), 0.78 (SFR), and 0.90 (SFR$/M_*$) with the $> 3\sigma$ significance levels. Next, we perform a linear fitting to the data points at all redshifts and at each redshift. The slopes of the lines at $z \sim 1$, 2, and 5–6 are fixed at the best-fit slope at $z \sim 0$, which is estimated as a free parameter. The best-fit results are illustrated in Figure 5. The best-fit slopes are positive for $v_{\rm cir}$, SFR, and SFR$/M_*$. The scatters of data points for $v_{\rm cir}$ and SFR is ~ 0.1 dex. However, the relation for SFR$/M_*$ at $z \sim 0$ (blue) have a large offset from that at $z \sim 5$–6 (red) and a large angle to $z \sim 0$–6 (black), in comparison with the relations for $v_{\rm cir}$ and SFR. Therefore, $v_{\rm cir}$ and SFR are likely to have the tightest single relations with $v_{\rm max}$ from $z \sim 0$ to 6.

The strong $v_{\rm max}$-correlations with $v_{\rm cir}$ and SFR imply a strong correlation between $v_{\rm cir}$ and SFR. To understand the SFR–$v_{\rm cir}$ relation independent of redshifts, it is helpful to see the distribution of the star-forming main-sequence galaxies on a SFR–$v_{\rm cir}$ plane. The top panel of Figure 6 illustrates the main sequences at $z \sim 0.5$, 1, 2, and 6 that are presented by Speagle et al. (2014). The galaxies in this work and Sugahara et al. (2017) have similar stellar masses in the range of $10.0 < \log(M_*/{\rm M}_\odot) < 11.0$. We note that the main sequence at $z \sim 0.5$ (blue line) agrees with galaxies at $z \sim 0.1$ (blue circles) since Sugahara et al. (2017) construct the $z \sim 0$ sample with the highly star-forming galaxies to analyze the Na I D absorption line. By converting M_* into $v_{\rm cir}$

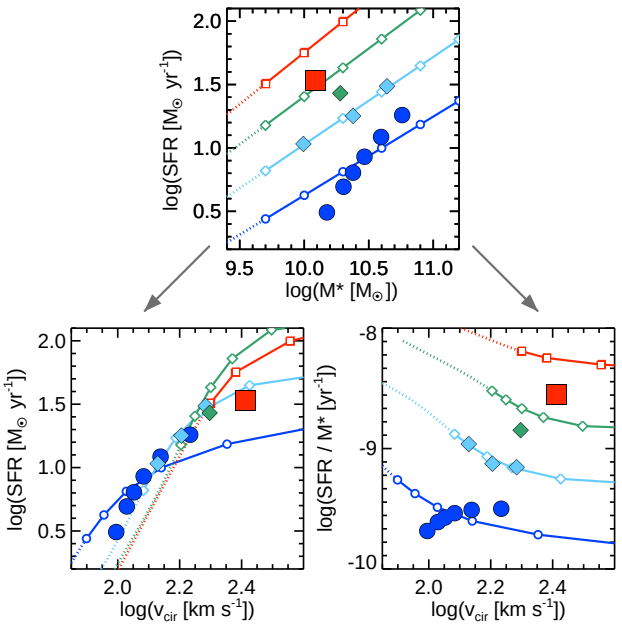

Figure 6. Models of the correlations of SFR and SFR/M_* with $v_{\rm cir}$ for the star-forming main-sequence galaxies. Top: main sequences at $z \sim 0.5$ (blue), 1 (cyan), 2 (green), and 6 (red) that are presented by Speagle et al. (2014). The open symbols on the solid lines are plotted at the intervals of 0.3 dex of M_* for reference. The main sequences are extrapolated to $\log(M_*/{\rm M}_\odot) < 9.7$, indicated by the dotted lines. The filled symbols are the same as in Figure 2. Bottom Left: SFR versus $v_{\rm cir}$ where $v_{\rm cir}$ is converted from M_* in the top panel using the SHMR in Behroozi et al. (2013). SFR correlates with $v_{\rm cir}$ over $z = 0$–6. Bottom Right: SFR/M_* versus $v_{\rm cir}$. The data points, which are in a similar M_* range, exhibit a positive correlation, but the solid lines demonstrate that the main-sequence galaxies at all redshifts do not exhibit a correlation between SFR/M_* and $v_{\rm cir}$.

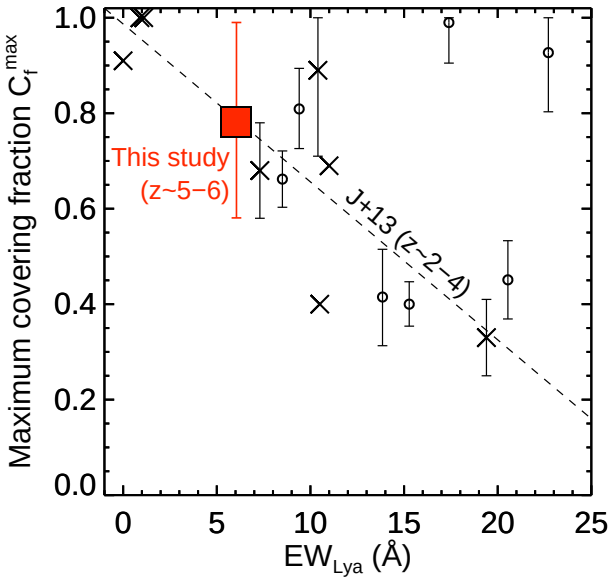

Figure 7. The maximum covering fraction $C_f^{\rm max}$ as a function of the Lyα equivalent width. The red square denotes the result at $z = 5$–6. The crosses and the open circles indicate the values of gravitationally-lensed sources at $z \sim 2$–4 (Jones et al. 2013) and $z \sim 4$–5 (Leethochawalit et al. 2016), respectively. The dashed line is the best-fit linear relation to the crosses (Jones et al. 2013).

with the method in Section 2, we show the main sequences on a SFR–$v_{\rm cir}$ plane in the bottom left panel of Figure 6. They show similar positive relations at all redshifts, leading to a positive correlation of the main-sequence galaxies, irrespective of redshifts. The data points indeed exhibit a strong positive correlation ($r = 0.99$) at the 5.8σ significance level. This result naturally explains a correlation between $v_{\rm max}$ and SFR, provided that $v_{\rm cir}$ determines $v_{\rm max}$ as shown in Figure 3. In addition, we plot the main sequences on a SFR/M_*–$v_{\rm cir}$ plane in the bottom right panel of Figure 6. Contrary to those in the SFR–$v_{\rm cir}$ plane, the main sequences show negative correlations and offsets in the positive direction from low to high redshifts. This demonstrates that the apparent positive correlation of the data points on the SFR/M_*–$v_{\rm cir}$ plane are simply because the galaxies have the similar stellar masses. We also check the main sequences on a $\Sigma_{\rm SFR}$–$v_{\rm cir}$ plane by assuming that galaxy sizes are proportional to redshifts by $(1+z)^{-1}$ (Shibuya et al. 2015), finding that the main sequences show a large dispersion, similarly to those on the SFR/M_*–$v_{\rm cir}$ plane.

The parameters which most strongly correlate with $v_{\rm max}$ are $v_{\rm cir}$ and SFR, suggesting that the fundamental parameter to determine the outflow velocity is $v_{\rm cir}$ or SFR. This result agrees with previous observational studies that present positive correlations of $v_{\rm max}$ with M_* (Martin 2005; Rubin et al. 2014; Erb et al. 2012) or SFR (Kornei et al. 2012; Heckman et al. 2015; Heckman & Borthakur 2016). In many cases, the outflow properties are assumed to be connected with star-forming activities in galaxies. However, $v_{\rm cir}$ affects SFR through the halo accretion rate (e.g., Harikane et al. 2017; Tacchella et al. 2018) and this process contributes to form the SFR–$v_{\rm cir}$ correlation in Figure 6. Thus, since $v_{\rm cir}$ represents two important parameters for the outflow velocity, the gravitational potential and the star-forming activity, it is important to consider the possibility that $v_{\rm cir}$ is the fundamental parameter to determine the outflow velocity.

5.3. *Lyman-continuum leakage*

The redshift $z = 5$–6 is near the end of the cosmic reionization, when the neutral IGM has been ionized. Plausible ionizing sources are young, low-mass galaxies (e.g., Robertson et al. 2015; Ishigaki et al. 2018), but their contribution is still a matter of debate. A key physical parameter is the escape fraction of the Lyman-continuum (LyC) photons from galaxies ($f_{\rm esc}$). It is possible that the outflows help increase

$f_{\rm esc}$ by creating holes in the neutral ISM from which the LyC photons can escape. However, direct measurements of $f_{\rm esc}$ are challenging for galaxies at $z = 5$–6 because the LyC photons almost disappear by ionizing the neutral IGM. In this section, we discuss the $f_{\rm esc}$ value of our galaxies at $z = 5$–6 with two indirect methods regarding the absorption lines.

In the first method, we calculate the covering fraction of the metal absorption lines. Assuming that the low-ionized elements are associated with the neutral-hydrogen gas, Jones et al. (2013) evaluate the maximum covering fraction ($C_f^{\rm max}$) of the low-ionized elements from the low-ionized absorption lines as an upper limit of $f_{\rm esc}$. Since our composite spectrum has the low continuum S/N, we define $C_f^{\rm max}$ as $C_f^{\rm max} = 1 - F_{\rm SiII}$, where $F_{\rm SiII}$ is the median flux density of the Si II line from -350 to -100 km s^{-1} in the normalized spectrum. Its error is calculated with the parametric bootstrap method based on the spectral noise. The measured value is $C_f^{\rm max} = 0.8 \pm 0.2$. We note that this $C_f^{\rm max}$ value is likely smaller than the value evaluated by the method in Jones et al. (2013) because our $C_f^{\rm max}$ value is calculated in the wide velocity range of 250 km s^{-1}. We additionally measure the Lyα equivalent width (EW$_{\rm Ly\alpha}$) of the composite spectrum to be EW$_{\rm Ly\alpha} = 6.05 \pm 0.45$ Å, using the emission strength from the stellar continuum at 1216–1221 Å.

Figure 7 illustrates $C_f^{\rm max}$ as a function of EW$_{\rm Ly\alpha}$. Our measurement at $z = 5$–6 (red square) is consistent with previous results (Jones et al. 2013; Leethochawalit et al. 2016) and on the linear relation at $z \sim 2$–4 presented by Jones et al. (2013, dashed line). This is the first observational result showing that the linear relation between $C_f^{\rm max}$ and EW$_{\rm Ly\alpha}$ holds even at $z > 5$, provided that the relation is independent of the stellar mass. Using the $C_f^{\rm max}$ value corresponding to EW$_{\rm Ly\alpha} = 6.05$ Å on the relation, we obtain an upper limit of $f_{\rm esc}$ to be $\simeq 0.2$. This secure upper limit is too weak to constrain models where bright galaxies contribute to the cosmic reionization (e.g., $\sim 10\%$; Sharma et al. 2017). However, Jones et al. (2013) emphasize that the property derived by this method is an upper limit. Following an equation derived by Chisholm et al. (2018), who propose indirect estimations of $f_{\rm esc}$ using local LyC leaking galaxies, we obtain $f_{\rm esc} \lesssim 0.5 - 0.6 C_f^{\rm max} = 0.02$. Hence, the intrinsic $f_{\rm esc}$ is likely much lower than the upper-limit value.

In the second method, we consider the shape of the absorption-line profile using the outflow velocities. Chisholm et al. (2017) calculate the ratio of the maximum outflow velocity to the central outflow velocity ($v_{90}/v_{\rm cen}$) of galaxies at $z = 0$. They find that the LyC leaking galaxies exhibit smaller ratios, $v_{90}/v_{\rm cen} \lesssim 5$, than galaxies without LyC leakage, although there are several galaxies with $v_{90}/v_{\rm cen} < 5$ but $f_{\rm esc} = 0$. Here we use $|v_{\rm max}/v_0|$ for an alternative to $v_{90}/v_{\rm cen}$ used in Chisholm et al. (2017). The ratio for the galaxies at $z = 5$–6 is obtained to be $|v_{\rm max}/v_0| = 2.0 \pm 0.2$. This result suggests that the galaxies at $z = 5$–6 are the LyC leaking galaxies, in contrast to the result of the first method. Further studies on both the LyC photons and the absorption-line properties will provide key quantities to address the challenge of estimating $f_{\rm esc}$ for galaxies at the epoch of reionization.

6. CONCLUSION

We study the outflow velocities of star-forming galaxies at $z = 5$–6 and discuss the redshift evolution of the outflow velocities from $z \sim 0$ to 6 by analyzing rest-frame FUV spectra of seven LBGs at $z = 5$–6 taken by DEIMOS available to date. We construct a high-S/N composite FUV spectrum based on the systemic redshifts determined by ALMA [C II] 158 μm observations (Capak et al. 2015) to fit a line profile to the Si II λ1260, C II λ1335, and Si IV $\lambda\lambda$1394, 1403 absorption lines. One of the best-fit parameters v_0, the central velocity of the line profile, is significantly negative, which implies that the absorption lines are blueshifted by the outflows.

The maximum outflow velocity $v_{\rm max}$ is measured from the best-fit parameters. The $v_{\rm max}$ values for the low-ionized lines (Si II and C II) are comparable to the one for the high-ionized line (Si IV), within the moderately large errors. By a simultaneous fit to the Si II and C II lines, we obtain $v_{\rm max} = 810^{+140}_{-160}$ km s^{-1}, which is higher than those at $z \sim 0$ and comparable to the one at $z \sim 2$ presented by Sugahara et al. (2017). This result represents the redshift evolution of $v_{\rm max}$ that strongly increases from $z \sim 0$ to 2 and weakly increases from $z \sim 2$ to 6, at the fixed stellar mass of $\log(M_*/{\rm M}_\odot) \sim 10.1$. We additionally measure the central outflow velocity ($v_{\rm out}$) by fitting a two-component Gaussian profile to the C II line, and confirm that the redshift evolution of $v_{\rm out}$ is similar to the $v_{\rm max}$ evolution.

Over $z \sim 0$–6, $\log v_{\rm max}$ is linearly correlated with the halo circular velocity ($\log v_{\rm cir}$) that are estimated from the stellar mass. This linear correlation can explain the increasing features of the $v_{\rm max}$ evolution because $v_{\rm cir}$ is proportional to $(1+z)^{0.5}$ for the galaxies with $\log M_* \sim 10.1$ M$_\odot$, at which the halo mass is almost constant over $z \sim 0$–6 (Behroozi et al. 2013). In addition, the correlation between $v_{\rm max}$ and $v_{\rm cir}$ is in good agreement with a relation predicted by the FIRE simulation (Muratov et al. 2015), suggesting that the multi-phase outflows are driven by a common $v_{\rm max}$–$v_{\rm cir}$ relation. The strong correlations of $v_{\rm max}$ with $v_{\rm cir}$ and SFR leads to the SFR–$v_{\rm cir}$ correlation, which is reproduced by the models of the star-forming main sequences at $z = 0$–6. Considering that $v_{\rm cir}$ has an impact on SFR through the halo accretion rate, it is possible that $v_{\rm cir}$ is the fundamental parameter to determine $v_{\rm max}$.

Absorption-line profiles are also used for indirect estimations of the escape fraction of the LyC photons ($f_{\rm esc}$). We measure the maximum covering fraction of the Si II line and the Lyα equivalent width of the composite spectrum, finding that the measured values at $z = 5$–6 are consistent with a relation at $z \sim 2$–4 found by Jones et al. (2013). The intrinsic $f_{\rm esc}$ would be much lower than the secure upper limit $f_{\rm esc} < 0.2$, while the ratio $|v_{\rm max}/v_0|$ is comparable to the values of the LyC leaking galaxies reported by Chisholm et al. (2017).

We thank Kate Rubin, John Chisholm, Léo Michel-Dansac, and Hidenobu Yajima for useful discussions. We acknowledge Peter Capak, the PI of the data in this work. The data presented herein were obtained at the W. M. Keck Observatory, which is operated as a scientific partnership among the California Institute of Technology, the University of California and the National Aeronautics and Space Administration. The Observatory was made possible by the generous financial support of the W. M. Keck Foundation. This research has made use of the Keck Observatory Archive (KOA), which is operated by the W. M. Keck Observatory and the NASA Exoplanet Science Institute (NExScI), under contract with the National Aeronautics and Space Administration. The authors wish to recognize and acknowledge the very significant cultural role and reverence that the summit of Maunakea has always had within the indigenous Hawaiian community. We are most fortunate to have the opportunity to conduct observations from this mountain. This work is supported by World Premier International Research Center Initiative (WPI Initiative), MEXT, Japan, and KAKENHI (15H02064, 17H01110, and 17H01114) Grant-in-Aid for Scientific Research (A) through Japan Society for the Promotion of Science. Y.S. acknowledges support from the JSPS through the JSPS Research Fellowship for Young Scientists.

REFERENCES

Abazajian, K. N., Adelman-McCarthy, J. K., Agüeros, M. A., et al. 2009, ApJS, 182, 543

Ajiki, M., Taniguchi, Y., Murayama, T., et al. 2002, ApJL, 576, L25

Behroozi, P. S., Wechsler, R. H., & Conroy, C. 2013, ApJ, 770, 57

Bouché, N., Hohensee, W., Vargas, R., et al. 2012, MNRAS, 426, 801

Capak, P. L., Carilli, C., Jones, G., et al. 2015, Nature, 522, 455

Chen, Y.-M., Tremonti, C. A., Heckman, T. M., et al. 2010, AJ, 140, 445

Chisholm, J., Orlitová, I., Schaerer, D., et al. 2017, A&A, 605, A67

Chisholm, J., Tremonti, C. A., Leitherer, C., & Chen, Y. 2016a, MNRAS, 463, 541

Chisholm, J., Tremonti, C. A., Leitherer, C., Chen, Y., & Wofford, A. 2016b, MNRAS, 457, 3133

Chisholm, J., Tremonti, C. A., Leitherer, C., et al. 2015, ApJ, 811, 149

Chisholm, J., Gazagnes, S., Schaerer, D., et al. 2018, A&A, 616, A30

Cooper, M. C., Newman, J. A., Davis, M., Finkbeiner, D. P., & Gerke, B. F. 2012, ASCL, ascl:1203.003

Du, X., Shapley, A. E., Reddy, N. A., et al. 2018, ApJ, 860, 75

Erb, D. K., Quider, A. M., Henry, A. L., & Martin, C. L. 2012, ApJ, 759, 26

Erb, D. K., Steidel, C. C., Shapley, A. E., et al. 2006, ApJ, 647, 128

Erb, D. K., Steidel, C. C., Trainor, R. F., et al. 2014, ApJ, 795, 33

Faber, S. M., Phillips, A. C., Kibrick, R. I., et al. 2003, in Proc. SPIE, Vol. 4841, Instrument Design and Performance for Optical/Infrared Ground-based Telescopes, ed. M. Iye & A. F. M. Moorwood, 1657–1669

Gallerani, S., Pallottini, A., Feruglio, C., et al. 2018, MNRAS, 473, 1909

Harikane, Y., Ouchi, M., Ono, Y., et al. 2017, ArXiv e-prints, arXiv:1704.06535

Hashimoto, T., Verhamme, A., Ouchi, M., et al. 2015, ApJ, 812, 157

Hashimoto, T., Inoue, A. K., Mawatari, K., et al. 2018, ArXiv e-prints, arXiv:1806.00486

Heckman, T. M., Alexandroff, R. M., Borthakur, S., Overzier, R., & Leitherer, C. 2015, ApJ, 809, 147. http://dx.doi.org/10.1088/0004-637X/809/2/147

Heckman, T. M., & Borthakur, S. 2016, ApJ, 822, 9

Heckman, T. M., Lehnert, M. D., Strickland, D. K., & Armus, L. 2000, ApJS, 129, 493

Ilbert, O., McCracken, H. J., Le Fèvre, O., et al. 2013, A&A, 556, A55

Inoue, A. K., Tamura, Y., Matsuo, H., et al. 2016, Science, 352, 1559

Ishigaki, M., Kawamata, R., Ouchi, M., et al. 2018, ApJ, 854, 73

Jones, T., Stark, D. P., & Ellis, R. S. 2012, ApJ, 751, 51

Jones, T. A., Ellis, R. S., Schenker, M. A., & Stark, D. P. 2013, ApJ, 779, 52

Kacprzak, G. G., Muzahid, S., Churchill, C. W., Nielsen, N. M., & Charlton, J. C. 2015, ApJ, 815, 22

Karman, W., Caputi, K. I., Caminha, G. B., et al. 2017, A&A, 599, A28

Kornei, K. A., Shapley, A. E., Martin, C. L., et al. 2012, ApJ, 758, 135

Leethochawalit, N., Jones, T. A., Ellis, R. S., Stark, D. P., & Zitrin, A. 2016, ApJ, 831, 152

Markwardt, C. B. 2009, in Astronomical Society of the Pacific Conference Series, Vol. 411, Astronomical Data Analysis Software and Systems XVIII, ed. D. A. Bohlender, D. Durand, & P. Dowler, 251

Martin, C. L. 2005, ApJ, 621, 227

Martin, C. L., Shapley, A. E., Coil, A. L., et al. 2012, ApJ, 760, 127

Mo, H. J., & White, S. D. M. 2002, MNRAS, 336, 112

Muratov, A. L., Kereš, D., Faucher-Giguère, C.-A., et al. 2015, MNRAS, 454, 2691

Muzahid, S., Kacprzak, G. G., Churchill, C. W., et al. 2015, ApJ, 811, 132

Newman, J. A., Cooper, M. C., Davis, M., et al. 2013, ApJS, 208, 5

Pavesi, R., Riechers, D. A., Capak, P. L., et al. 2016, ApJ, 832, 151

Reddy, N. A., Steidel, C. C., Pettini, M., et al. 2008, ApJS, 175, 48
Robertson, B. E., Ellis, R. S., Furlanetto, S. R., & Dunlop, J. S. 2015, ApJL, 802, L19
Rubin, K. H. R., Prochaska, J. X., Koo, D. C., et al. 2014, ApJ, 794, 156
Rupke, D. S., Veilleux, S., & Sanders, D. B. 2005a, ApJS, 160, 87
—. 2005b, ApJS, 160, 115
Schroetter, I., Bouché, N., Péroux, C., et al. 2015, ApJ, 804, 83
Schroetter, I., Bouché, N., Wendt, M., et al. 2016, ApJ, 833, 39
Scoville, N., Aussel, H., Brusa, M., et al. 2007, ApJS, 172, 1
Shapley, A. E., Steidel, C. C., Pettini, M., & Adelberger, K. L. 2003, ApJ, 588, 65
Sharma, M., Theuns, T., Frenk, C., et al. 2017, MNRAS, 468, 2176
Shibuya, T., Ouchi, M., & Harikane, Y. 2015, ApJS, 219, 15
Shibuya, T., Ouchi, M., Nakajima, K., et al. 2014, ApJ, 788, 74
Somerville, R. S., & Davé, R. 2015, ARA&A, 53, 51
Speagle, J. S., Steinhardt, C. L., Capak, P. L., & Silverman, J. D. 2014, ApJS, 214, 15
Steidel, C. C., Adelberger, K. L., Shapley, A. E., et al. 2003, ApJ, 592, 728
Steidel, C. C., Erb, D. K., Shapley, A. E., et al. 2010, ApJ, 717, 289
Steidel, C. C., Shapley, A. E., Pettini, M., et al. 2004, ApJ, 604, 534
Steinhardt, C. L., Speagle, J. S., Capak, P., et al. 2014, ApJL, 791, L25
Sugahara, Y., Ouchi, M., Lin, L., et al. 2017, ApJ, 850, 51
Tacchella, S., Bose, S., Conroy, C., Eisenstein, D. J., & Johnson, B. D. 2018, ApJ, 868, 92
Trainor, R. F., Steidel, C. C., Strom, A. L., & Rudie, G. C. 2015, ApJ, 809, 89
Veilleux, S., Cecil, G., & Bland-Hawthorn, J. 2005, ARA&A, 43, 769
Weiner, B. J., Coil, A. L., Prochaska, J. X., et al. 2009, ApJ, 692, 187